Spin-orbit interaction of light in three-dimensional microcavities

Jakob Kreismann [1,*] and Martina Hentschel[2]

[1]*Theoretical Physics II/Computational Physics Group, Institute for Physics, Technische Universität Ilmenau, Weimarer Straße 25, 98693 Ilmenau, Germany*

[2]*Institute of Physics, Faculty of Natural Sciences, Technische Universität Chemnitz, Reichenhainer Straße 70, 09126 Chemnitz, Germany*

(Received 16 July 2020; accepted 28 September 2020; published 23 October 2020)

We investigate the spin-orbit coupling of light in three-dimensional cylindrical and tubelike whispering gallery mode resonators. We show that its origin is the transverse confinement of light in the resonator walls, even in the absence of inhomogeneities or anisotropies. The spin-orbit interaction results in elliptical far-field polarization (spin) states and causes spatial separation of polarization handedness in the far field. The ellipticity and spatial separation are enhanced for whispering gallery modes with higher excitation numbers along the resonator height. We analyze the asymmetry of the ellipticity and the tilt of the polarization orientation in the far field of conelike microcavities. Furthermore, we find a direct relationship between the tilt of the polarization orientation in the far field and the local inclination of the resonator wall. Our findings are based on finite-difference time-domain simulations and are supported by three-dimensional diffraction theory.

DOI: 10.1103/PhysRevA.102.043524

I. INTRODUCTION

Mircooptical systems, which confine light to small volumes, have received a great deal of interest in recent decades [1,2]. Well-known examples of such systems include microspheres [3–5], microtoroids [6,7], and microdisks [8,9]. In particular, bottlelike and tubelike microcavities have received much attention in recent years [10–17]. In contrast to rather flat microdisks, these types of cavities allow a full three-dimensional (3D) formation of the resonances. Three-dimensional whispering gallery modes (WGMs) have been studied theoretically in, e.g., [10,18–24].

One aspect of interest is the polarization evolution in 3D microcavities, where, unlike the two-dimensional situation, the polarization directions do not decouple. This enables a coupling between the light's orbital motion in the resonator and its polarization (spin of light) state that is known as the spin-orbit interaction of light [25–27]. It has been studied in different contexts [24,28–33], with particular focus given to asymmetric microcavities and the role of anisotropies or inhomogeneities [15] as well as the interpretation in terms of geometric phases [34–37].

Here we investigate the spin-orbit interaction of light in symmetric and asymmetric photonic microsystems that are deduced from ringlike (hollow-cylinder-type) microcavities. The generic resonances are known to be whispering-gallery-type modes. The focus of this paper is the investigation of their spin-orbit interaction in dependence on the resonator geometry: How is the polarization state of light affected by inclining the resonator wall and manipulating its thickness and what role do the resonance morphology and excitation number play? Special attention will be given to the far-field polarization properties as this allows for a direct observation of our findings and their use in potential applications such a sensors or polarizers.

Whereas numerical finite-difference time-domain (FDTD) simulations will play a major role throughout the paper, we will see that optics in the form of Kirchhoff's diffraction theory yields valuable insight and understanding of the simulation results. This implies, however, that an explanation based geometric phases cannot be the objective of this paper. Though we will see manifold examples of the interplay between the resonator geometry and the resulting polarization evolution of light throughout this paper, the well-known explanation in terms of geometric phases and solid angles spanned in parameter space (which also applies, e.g., to spin-dependent transport of electrons along rings subject to inhomogeneous magnetic fields [38–41]) is not sufficient to capture the more complex situation that includes transformation into the far field we are interested in here.

The paper is organized as follows. In Sec. II we will recap the theory of the spin-orbit interaction of light applied to a WGM in a 3D dielectric ring resonator and in Sec. III apply it to an azimuthally propagating mode and its far-field emission. In Sec. IV we will study 3D WGMs in conelike tube cavities. As in the previous section, we will investigate the far-field polarization states and explain differences from the previous case. In Sec. V we study the role of inhomogeneous resonator wall structures. We summarize in Sec. VI. In Appendix A we give a short description of the FDTD method used. The results of vector diffraction theory that are used throughout this work are explained and summarized in Appendix B.

II. SPIN-ORBIT COUPLING OF LIGHT

We start the theoretical description of 3D optical microcavities by recapping Gauss' s law in differential form [42] for

*jakob.kreismann@tu-ilmenau.de

time-harmonic fields in dielectric media without free electric charges $\nabla \cdot [\varepsilon(\mathbf{r})\mathbf{E}(\mathbf{r})] = 0$, where $\varepsilon(\mathbf{r})$ describes an inhomogeneous dielectric material permittivity, $\mathbf{E}(\mathbf{r})$ represents the electric field vector, and $\mathbf{r}$ is the spatial coordinate. Applying the chain rule and rearranging terms leads to

$$\nabla \cdot \mathbf{E} = -\frac{1}{\varepsilon(\mathbf{r})}[\nabla\varepsilon(\mathbf{r})] \cdot \mathbf{E}. \tag{1}$$

This implies that the divergence of the electric field does not generally vanish (as it does in vacuum or homogeneous materials). Rather, it will take a finite value that depends on the orientation of the electric field with respect to the gradient of the permittivity. In cylindrical coordinates, Eq. (1) reads

$$\frac{1}{r}\partial_r(rE_\mathrm{r}) + \frac{1}{r}\partial_\phi E_\phi + \partial_z E_\mathrm{z} = -\frac{1}{\varepsilon(\mathbf{r})}\left(\varepsilon'_\mathrm{r}E_\mathrm{r} + \frac{\varepsilon'_\phi}{r}E_\phi + \varepsilon'_z E_\mathrm{z}\right),$$

with r the distance from the (cylinder) z axis, ∂_r the partial derivative with respect to r, and $\varepsilon'_{r(\phi,z)} = \partial_{r(\phi,z)}\varepsilon(\mathbf{r})$.

We now investigate a mode that is propagating in the ϕ direction, cyclically guided by a thin dielectric ring with constant mean radius $r = R$. Hence, the ϕ component is the longitudinal component, whereas the r and z components correspond to transverse (tr) components. Sorting by components yields

$$\frac{1}{R}\left(\partial_\phi E_\phi + \frac{\varepsilon'_\phi}{\varepsilon}E_\phi\right) = -\left(\nabla_\mathrm{tr} \cdot \mathbf{E}_\mathrm{tr} + \frac{1}{\varepsilon}(\nabla_\mathrm{tr}\varepsilon) \cdot \mathbf{E}_\mathrm{tr}\right). \tag{2}$$

We see that the longitudinal component E_ϕ and its change depend on the transverse confinement (first term on the right-hand side) and the transverse gradient of the material permittivity (second term on the right-hand side). In other words, an initially purely transverse field can induce a longitudinal component. This action of the light field orbit on its overall polarization is known as the spin-orbit interaction.

The complete electric field vector reads

$$\mathbf{E}(r, \phi, z) = (E_\mathrm{r}\mathbf{e}_\mathrm{r} + E_\phi\mathbf{e}_\phi + E_\mathrm{z}\mathbf{e}_\mathrm{z}) \tag{3}$$

$$= [A_\mathrm{r}(r, z)\mathbf{e}_\mathrm{r} + A_\phi(r, z)\mathbf{e}_\phi + A_\mathrm{z}(r, z)\mathbf{e}_\mathrm{z}]e^{im\phi}, \tag{4}$$

where the amplitudes A_r and A_z represent the transverse mode profile, A_ϕ is the longitudinal amplitude, and m is the azimuthal mode number. The $e^{im\phi}$ factor indicates an azimuthally traveling wave.

Applying Eq. (2) to the complete electric field vector of the mode and expanding a fraction yields

$$E_\phi = i\frac{R}{m}\frac{1}{1 - i\xi}\left(\nabla_\mathrm{tr} \cdot \mathbf{E}_\mathrm{tr} + \frac{1}{\varepsilon}(\nabla_\mathrm{tr}\varepsilon) \cdot \mathbf{E}_\mathrm{tr}\right), \tag{5}$$

where $\xi = \frac{1}{m}\frac{\varepsilon'_\phi}{\varepsilon}$ is a parameter describing how strong the material properties (components of the permittivity ε or the related refractive index n with $\varepsilon = n^2$) change along the ϕ direction with respect to the azimuthal mode number m. Equation (5) describes the spin-orbit interaction of light in WGMs. The orbital momentum of the mode represented by m is transformed into a (phase-shifted) spin momentum, the polarization, represented by E_ϕ. The spin-orbit interaction depends on the transverse confinement $\nabla_\mathrm{tr} \cdot \mathbf{E}_\mathrm{tr}$, the transverse material gradient $\nabla_\mathrm{tr}\varepsilon$, and material change ξ along the propagation direction ϕ. In particular, starting from a TE-like WGM where the transverse electric field is aligned (almost) parallel to the resonator wall $\mathbf{E}_\mathrm{tr} \approx E_\mathrm{z}\mathbf{e}_\mathrm{z}$, we find that spin-orbit coupling induces an E_ϕ component proportional to the derivative of E_z, $E_\phi \propto \partial E_\mathrm{z}/\partial z$.

If there is no ($\xi = 0$) or only weak material change ($\xi \ll 1$) along the ϕ direction, the prefactor reduces to iR/m. That is, the longitudinal component undergoes a phase shift of $\pi/2$ or a factor i. As a consequence, the propagating mode is elliptically polarized with the polarization ellipse lying in a plane spanned by $\mathbf{e}_\mathrm{z}$ and $\mathbf{e}_\phi$.

We will now briefly analyze under which conditions an originally linearly polarized mode can reach the limiting case of circular polarization, that is, equal longitudinal and transverse amplitudes $|E_\phi| \sim |\mathbf{E}_\mathrm{tr}|$. This requires

$$\frac{1}{2\pi}\frac{\lambda}{n}\frac{\nabla_\mathrm{tr} \cdot \mathbf{E}_\mathrm{tr}}{|\mathbf{E}_\mathrm{tr}|} \overset{!}{=} 1 \quad \text{or} \quad \frac{1}{2\pi}\frac{\lambda}{n}\frac{|\nabla_\mathrm{tr}\varepsilon|}{\varepsilon} \overset{!}{=} 1, \tag{6}$$

where we approximated the term R/m (cf. Eq. [5]) by $\lambda/2\pi n$ by applying the resonance condition $2\pi R \approx m\lambda/n$ of a WGM, with λ/n the medium wavelength. In order to fulfill the first condition of Eq. (6), the normalized change of the amplitude of the transverse electric field on the medium wavelength scale has to be of the order of 2π. This corresponds, however, to confinement of light on a scale of the medium wavelength. Such a strong confinement can be realized by highly focused beams, as recently investigated in [31], or WGM resonances in tubelike or bottlelike cavities (see [10–14,16,17,43,44]).

The second condition of Eq. (6) requires the normalized transverse permittivity of the material to change by a factor of $2\pi\varepsilon$ over one medium wavelength. Even for low refractive indices like $n = 1.2$ ($\varepsilon = 1.44$), this requires a permittivity change by the factor of 9 on the wavelength scale. At interfaces of different material, strong material gradients may occur, but these gradients are localized in the region of the material interface. For pure dielectric materials, a continuously strong permittivity change requires strong material inhomogeneities. We leave this to another study and focus here on homogeneous materials with strong transverse confinement of light such as in the walls of 3D-ring resonators. We will see that this generic situation can induce substantial spin-orbit coupling with a number of different effects.

This applies in particular to the observation of light in the far field. Therefore, we link now the fields inside the resonator to the far-field polarization states. Note that the electromagnetic radiation $\mathbf{E}_\mathrm{FF}$ at a distance r_FF in the far field has to be an outgoing wave

$$\mathbf{E}_\mathrm{FF} = (E_\varphi\mathbf{e}_\varphi + E_\theta\mathbf{e}_\theta)\exp(i\mathbf{k} \cdot \mathbf{r}_\mathrm{FF} - i\omega t), \tag{7}$$

where $\mathbf{e}_\varphi$ and $\mathbf{e}_\theta$ are the unit vectors in the directions of φ and θ, respectively, as known from spherical coordinates. Both are perpendicular (transverse) to the propagation direction $\mathbf{k}/|\mathbf{k}|$. Here E_φ and E_θ are the corresponding φ and θ components.

In a local far-field coordinate system $(\tilde{x}, \tilde{z})$, where the $\tilde{x}$ axis and $\tilde{z}$ axis are spanned by $\mathbf{e}_\varphi$ and $\mathbf{e}_\theta$, respectively, the physically observable electric field given by the real part of $\mathbf{E}_\mathrm{FF}$ describes an ellipse in general [see Fig. 1(a)]. This polarization ellipse is characterized by (i) the orientation angle Ψ of its major axis with respect to the $\tilde{z}$ axis, (ii) the ellipticity angle χ (with $\tan\chi =$ minor axis/major axis), and (iii) the handedness σ of the direction of rotation of $\mathrm{Re}[\mathbf{E}_\mathrm{FF}]$ when

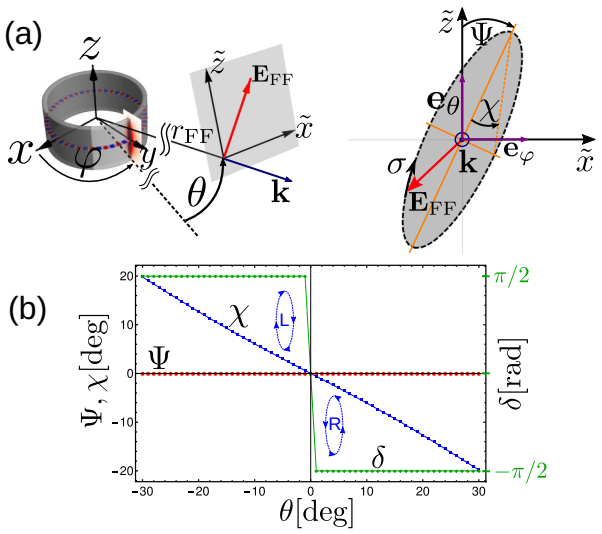

FIG. 1. Far-field polarization properties. (a) Characterization of the far-field polarization state by Ψ, the angle of orientation; χ, the ellipticity angle; and σ, the handedness. (b) Plot of Ψ and χ of a 3D-ring WGM far field derived from the Kirchhoff diffraction formula for the fundamental axial mode ($q = 1$). See the text for details.

looking against the propagation direction (looking towards the resonator) (see Fig. 1).

The quantities Ψ, χ, and σ are given by [45]

$$\tan 2\Psi = \frac{2\nu}{1-\nu^2}\cos\delta, \tag{8}$$

$$\sin 2\chi = \frac{2\nu}{1+\nu^2}\sin\delta, \tag{9}$$

$$\sigma = \mathrm{sgn}(\delta), \tag{10}$$

where $\nu = A_\varphi/A_\theta$ is the ratio of the amplitudes of the far-field components E_φ and E_θ and $\delta = \arg(E_\varphi/E_\theta)$ represents the phase difference between E_φ and E_θ. The angle Ψ describes the tilt with respect to the local $\tilde{z}$ axis and ranges from $-90°$ to $+90°$. In addition, $\Psi = 0°$ and $\Psi = 90°$ correspond to vertical (parallel to the $\tilde{z}$ axis) and horizontal (parallel to the $\tilde{x}$ axis) polarization orientations, respectively. The ellipticity angle χ describes the states of linear ($\chi = 0°$), elliptical ($0° < |\chi| < 45°$), and circular ($|\chi| = 45°$) polarization. The sign of χ corresponds to the sign of the phase difference δ because of the $\sin\delta$ term in Eq. (9). Further, $\chi < 0$ and $\chi > 0$ represent right-handed ($\sigma = -1$) and left-handed ($\sigma = +1$) polarization, respectively.

The desired relation between the fields inside the ring resonator (E_ϕ, E_z) and the far-field components (E_φ, E_θ) is provided by the Kirchhoff diffraction theory that we explain in more detail in Appendix B. To this end we treat the sidewall of the 3D-ring resonator as an aperture that diffracts the fields of the WGM resonances into the far field. Due to the thin-wall structure, we approximate the 3D ring by a cylinder surface S of radius R and height h. The electric far-field vector $\mathbf{E}_{\mathrm{FF}}$ can be computed by evaluating Kirchhoff's vector diffraction formula in the Fraunhofer (or far-field) limit [42], yielding

$$\mathbf{E}_{\mathrm{FF}} \sim \mathbf{k} \times \iint_S \mathbf{n}' \times \mathbf{E}(\mathbf{x}')\exp(-i\mathbf{k}\cdot\mathbf{x}')da', \tag{11}$$

where $\mathbf{x}'$ is the position vector on the diffracting surface S with area element $da' = dz'Rd\phi' = hdu'Rd\phi'$ and electric field $\mathbf{E}(\mathbf{x}')$, $\mathbf{n}'$ is the unit vector normal to the surface, and $\mathbf{k}$ is the far-field wave vector. Note that only fields parallel to the surface S [represented by the term $\mathbf{n}' \times \mathbf{E}(\mathbf{x}')$ in Eq. (11)] are considered. Contributions from normal field components, proportional to $\mathbf{n}' \cdot \mathbf{E}(\mathbf{x}')$, which would show up as an additional magnetic field term inside Eq. (11), were neglected because the predominantly TE-like character of the WGM resonances ensures the electric field components to be parallel to the resonator wall and thus parallel to the diffracting surface S. The fields at the cylindrical diffracting surface can be represented as $\mathbf{E}(\mathbf{x}') = [A_z(z')\mathbf{e}_z + A_\phi(z')\mathbf{e}_\phi]\exp(im\phi')$.

Evaluating the diffraction formula (11), we obtain the sought-after expressions for the far-field components E_φ and E_θ (see Appendix B 1),

$$E_\varphi(\varphi,\theta) = hR\exp(im\varphi)\exp\left(-i\frac{\pi}{2}m\right)J_m(\tilde{k}_1) \times \left(\hat{A}_z(\tilde{k}_2)\frac{\tilde{k}_1^2 - m^2}{m\tilde{k}_1}\sin\theta - \Delta\cos\theta\right), \tag{12}$$

$$E_\theta(\varphi,\theta) = hR\exp(im\varphi)\exp\left(-i\frac{\pi}{2}(m+1)\right) \times \hat{A}_z(\tilde{k}_2)\frac{J_{m-1}(\tilde{k}_1) - J_{m+1}(\tilde{k}_1)}{2}, \tag{13}$$

where the J_μ are the Bessel functions of the first kind with $\tilde{k}_1 = kR\cos\theta$ and $\tilde{k}_2 = kh\sin\theta$. In addition, $\hat{A}_z(\tilde{k}_2)$ and Δ represent the expressions using $dz' = hdu'$,

$$\hat{A}_z(\tilde{k}_2) = \int_{-1/2}^{1/2}\tilde{A}_z(u')\exp(-i\tilde{k}_2u')du', \tag{14}$$

$$\Delta = \frac{i}{m}\frac{R}{h}\tilde{A}_z(u')\exp(-i\tilde{k}_2u')\Big|_{u_1'=-1/2}^{u_2'=1/2} = \frac{2R}{mh}\tilde{A}_z(\tfrac{1}{2}) \times \begin{cases}\sin(\frac{\tilde{k}_2}{2}) & \text{for } q = 1,3,5,\ldots\\ i\cos(\frac{\tilde{k}_2}{2}) & \text{for } q = 2,4,6,\ldots,\end{cases} \tag{15}$$

where Eq. (14) resembles the diffraction pattern of a slit of height h with the local amplitude $\tilde{A}_z(u')$. Due to the strong confinement, the amplitude $\tilde{A}_z(u')$ rapidly converges towards zero above and below the wall of the ring as shown in Fig. 2, and therefore $\hat{A}_z(\tilde{k}_2)$ can be interpreted as the Fourier transform of $\tilde{A}_z(u')$. Equation (15) describes an additional term taking the amplitude $\tilde{A}_z$ at the upper and lower boundaries into account where q represents the axial mode number (cf. Sec. III). It arises from integration by parts of the $\tilde{A}_\phi(u')$ component ($\tilde{A}_\phi \propto \partial\tilde{A}_z/\partial u'$) (cf. Appendix B 1).

For the sake of simplicity, we neglect the boundary amplitude in Eq. (15) for the fundamental axial mode ($q = 1$), $\tilde{A}_z(\frac{1}{2}) = \tilde{A}_z(-\frac{1}{2}) \approx 0$. As a result, $\Delta = 0$ and we see that the E_φ and E_θ components of the far field [Eqs. (12) and (13)] are directly connected to the Fourier transform of the E_z component of the WGM field at the resonator wall. Furthermore, the E_φ component changes its sign at $\theta = 0$ because of the $\sin\theta$ term, which indicates far-field polarization states of opposite handedness for $\theta < 0$ and $\theta > 0$. Remarkably, the polarization quantities Ψ and χ of the fundamental axial mode ($q = 1$) are independent of the far-field pattern represented by $\hat{A}_z(\tilde{k}_2)$ because this term cancels out in the parameter ν

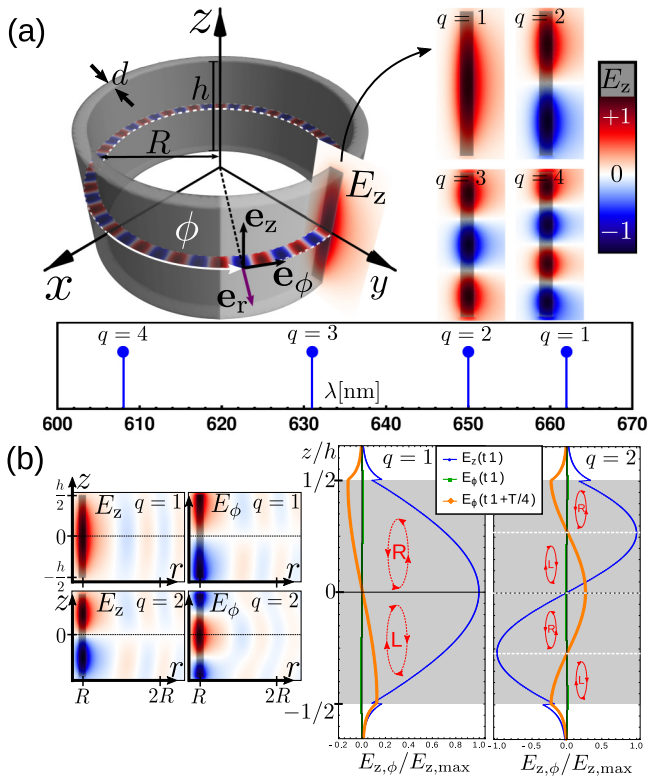

FIG. 2. Geometry and WGM. (a) Illustration of a cylindrical ring of thickness d and corresponding WGMs, and spectrum of the modes with different vertical excitations. The parameters are the azimuthal number $m = 24$, mean radius $R = 2\ \mu$m, height $h = R = 2\ \mu$m, wall thickness $d = 0.2\ \mu$m, and refractive index $n = 1.5$. (b) Shown on the left is the field distribution of E_z and E_ϕ in the exterior space ($r > R$) of the ring and on the right E_z and E_ϕ at $r = R$ as a function of z. See the text for details.

and it is also irrelevant for the phase difference δ. Thus, the spatial splitting of the handedness of the far-field polarization states, as illustrated in Fig. 1(b), is an intrinsic feature of a propagating (nonstanding) WGM.

For higher axial modes ($q > 1$), the contribution of Δ increases because of increasing boundary amplitudes (cf. Fig. 2) and will enhance the ellipticity χ as shown in the results further below. The fundamental feature of spatial splitting of the far-field polarization handedness is also enhanced.

III. CYLINDRICAL 3D-RING RESONATORS

We begin our study of spin-orbit interaction of light in a 3D-ring-resonator cavity with mean radius R, wall thickness d, and height h. The electromagnetic eigenmodes of such cavities are WGMs (hosted in the cavity cross section) subject to the additional confinement in the z direction [see Fig. 2(a)]. The field pattern of E_z exhibits different types of excitations that can be characterized by the axial mode number q representing the number of extrema of E_z along the resonator height.

Figure 2(a) illustrates the ring geometry and slices of the 3D field distribution E_z at $z = 0$ (showing the radial and azimuthal distribution of the field) and at $x = 0$ (showing its vertical distribution). The field distributions are taken from a temporal snapshot of a clockwise propagating wave with $m = 24$ and $q = 1$. The panel on the right-hand side shows the fundamental vertical excitation $q = 1, 2, 3, 4$ and the lower panel their spectral positions, indicating that the wavelength decreases with increasing excitation as expected.

The diagrams on the right-hand side of Fig. 2(b) show the transverse E_z and the longitudinal component E_ϕ of the electric field of the fundamental mode $q = 1$ and the first vertical excitation $q = 2$ at two different time steps t_1 and $t_1 + \frac{T}{4}$, with T the optical period. The fields are taken along the center of the wall ($r = R$) (cf. the insets on the left-hand side).

We see that the graphs of E_ϕ correspond to the derivative of E_z [cf. Eq. (5)]. Furthermore, we see that E_ϕ reaches its maximum a quarter period later than E_z because of the factor i resulting from the confinement of the propagating mode [cf. Eq. (5) with $\xi = 0$]. This phase shift of $\pi/2$ generates elliptical polarization inside the ring resonator as illustrated by the red ellipses. Note that the polarization ellipse lies in a plane spanned by $\mathbf{e}_z$ and $\mathbf{e}_\phi$, that is, the polarization ellipse lies parallel to the propagation direction. The upper (lower) half of the $q = 1$ WGM carries right-handed (left-handed) elliptical polarization where right-handed (left-handed) elliptical or circular polarization is defined by the opposite (same) sign of the E_z and E_ϕ components.

As we will see below, precisely this splitting is transferred into the far field and can be observed there. The $q = 2$ WGM has four regions [separated by horizontal dashed lines in Fig. 2(b)] of alternating right- and left-handed polarization. We point out that elliptical polarization occurs in traveling waves only, whereas in standing-wave WGMs the transverse spin momenta of the counterpropagating modes cancel exactly and yield linear polarization.

In the next step, we will investigate how the far-field polarization state depends on (i) the far-field (observation) angle and (ii) the vertical excitation number q. The far fields were obtained by computing the far-field electric field vector $\mathbf{E}^{\mathrm{FF}}$ and its far-field components E_φ and E_θ at a distance of $r_{\mathrm{FF}} = 50\ \mu$m from the origin [see the inset of Fig. 3(a)]. The angles φ and θ are the azimuthal and elevation angle of the far field, respectively. The far-field polarization states are characterized by the orientation angle Ψ, the ellipticity angle χ, and the handedness σ [cf. Fig. 1(a)].

Due to the rotational symmetry around the z axis, the φ dependence is trivial and thus we focus on the θ dependence of the far field. Figure 3(a) shows the far-field intensity $|\mathbf{E}^{\mathrm{FF}}(\theta)|^2$ as a polar plot for $q = 1, 2$ and $q = 3, 4$, respectively. We find that q corresponds directly to the number of observed far-field lobes. This connection can be explained by Fraunhofer (far-field) diffraction where the wall of the resonator acts as an aperture [see Eq. (11)]. The dominant E_z component of the WGM resonance will also rule the far-field pattern.

In Fig. 3(a) the far-field electric field vector in the local $\tilde{x}$-$\tilde{z}$ coordinate system is shown at the elevation angles θ with maximum far-field emission (and $\theta = \pm 11^\circ$ for $q = 1$) indicated on top of each frame. From top to bottom, the $q = 1, 2, 3, 4$ cases are shown. The electric field vectors are taken over one oscillation period where the red arrows and

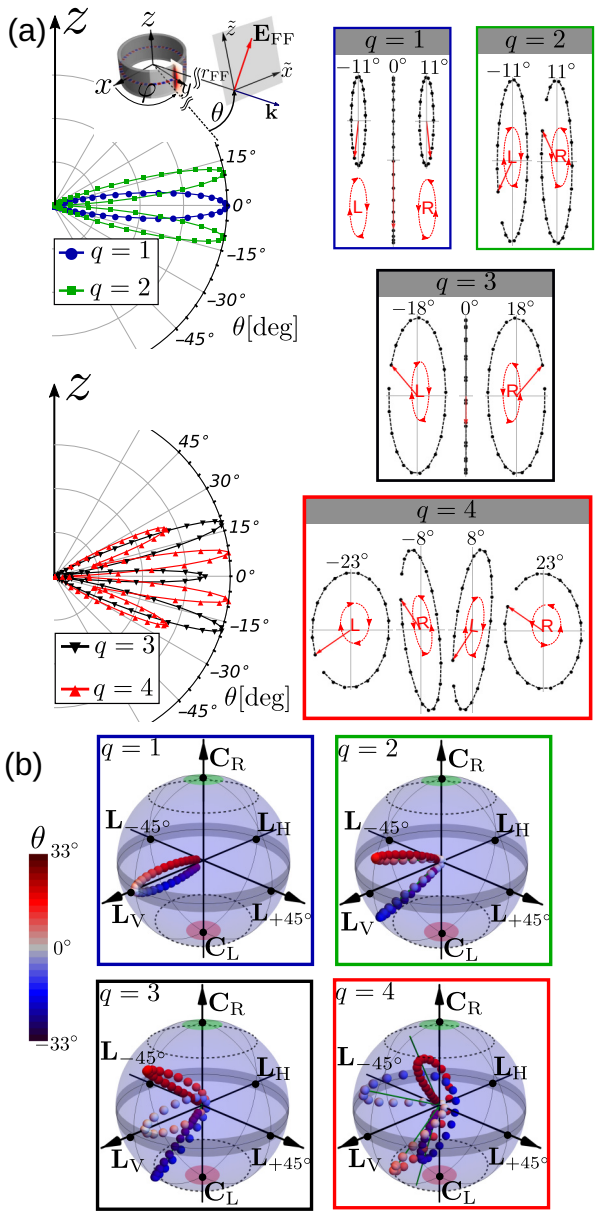

FIG. 3. Far fields and far-field polarization states. (a) Polar plots of far-field intensities of different vertical excitation numbers q. The frames show the polarization ellipses along the (maximum) far-field direction θ indicated above each ellipse. (b) Poincaré spheres of polarization displaying observable polarization states when scanning the far field within the given θ range. See the text for details.

black dots correspond to the phase-dependent position of the first snapshot and the 19 following snapshots of the oscillation period, respectively.

In the case of the $q = 1$ WGM, we observe left-handed (right-handed) elliptical polarization for negative (positive) far-field angles θ and linear polarization at the lobe maximum at $\theta = 0$. This separation of the polarization handedness in the far field arises from the reversed polarization distributions inside the resonator [cf. Fig. 2(b)]. The maximum of the lobe at $\theta = 0°$ shows linear polarization because the $z = 0$ plane is a symmetry (mirror) plane at which the opposite-handed polarization states compensate each other, resulting in linear polarization pointing into the z direction, i.e., $\Psi = 0°$. Similar results of polarization separation in the far field were observed for scattering of surface plasmons at nanostructures [29].

The far field of the $q = 2$ WGM has two pronounced lobes with opposite polarization handedness and stronger elliptical polarization compared to the $q = 1$ case. The more pronounced elliptical polarization arises from the stronger confinement along the z direction of the $q = 2$ mode, and hence a stronger spin-orbit interaction generating a stronger E_ϕ component as shown in Fig. 2(b) (the maximum of $E_\phi/E_{z,\max}$ for $q = 2$ reaches almost 0.3, whereas $E_\phi/E_{z,\max}$ for $q = 1$ remains below 0.2). The two far-field lobes arise from the dominant E_z component [cf. Fig. 2(b)], whereas the opposite handedness results from the opposite polarization distribution inside the resonator.

For $q = 3$, the far field is very similar to the one of $q = 1$ because in both cases it has an even E_z and odd E_ϕ distribution inside the resonator. The stronger pronounced elliptical polarization arises from the now even stronger confinement as explained for the $q = 2$ case.

Eventually, the far field of the $q = 4$ WGM shows four lobes of alternating polarization handedness and switching ellipticity. The outer lobes show almost circular polarization. The polarization orientation of the inner lobes is slightly tilted from the z axis.

In order to further characterize the polarization states, we use their Ψ and χ values to present them on the so-called Poincaré sphere of polarization [45] [cf. Fig. 3(b)]. The sphere is spanned by 2Ψ and 2χ, which represent the azimuthal and elevation angles, respectively. The equator of this sphere ($\chi = 0$) corresponds to linear polarization states of different orientations: $2\Psi = 0$, linear vertical ($\mathbf{L}_\mathrm{V}$); $2\Psi = \pi$, linear horizontal ($\mathbf{L}_\mathrm{H}$); and $2\Psi = \pm\pi/2$, linear inclined by $\pm 45°$ ($\mathbf{L}_{\pm 45°}$). The poles of the Poincaré sphere at $2\chi = \pm\pi/2$ correspond to right-handed ($\mathbf{C}_\mathrm{R}$) and left-handed ($\mathbf{C}_\mathrm{L}$) circular polarization. All other states indicate elliptical polarization. The distance from the origin indicates the far-field intensity.

The Poincaré spheres in Fig. 3(b) illustrate the observable far-field polarization states when scanning the far field through the color-encoded θ range. For $q = 1, 2, 3$ the polarization handedness is directly related to different spatial regions θ as is clearly visible by the blue (red) points remaining in the lower (upper) hemisphere.

We emphasize that the far-field polarization ellipse lies in a plane spanned by $\mathbf{e}_\varphi$ and $\mathbf{e}_\theta$ and is transverse to the propagation direction $\mathbf{k}/|\mathbf{k}|$, whereas the polarization ellipse inside the resonator is longitudinal to the propagation direction $\mathbf{e}_\phi$. Thus, we observe a transition from a longitudinal to a transverse polarization ellipse orientation in the far field.

IV. CONELIKE 3D-RING RESONATORS

We now investigate the role of inclined resonator walls in order to understand 3D systems like conelike tube cavities or realistic (imperfect) 3D microresonators. The inclination angle γ of the resonator wall with respect to the z axis is illustrated in the inset of Fig. 4(a). Choosing $\gamma > 0°$ breaks the symmetry with respect to the $z = 0$ plane. As a consequence, we expect that the modes inside the resonator and the far-field lobes will display an asymmetry as well. Analyzing

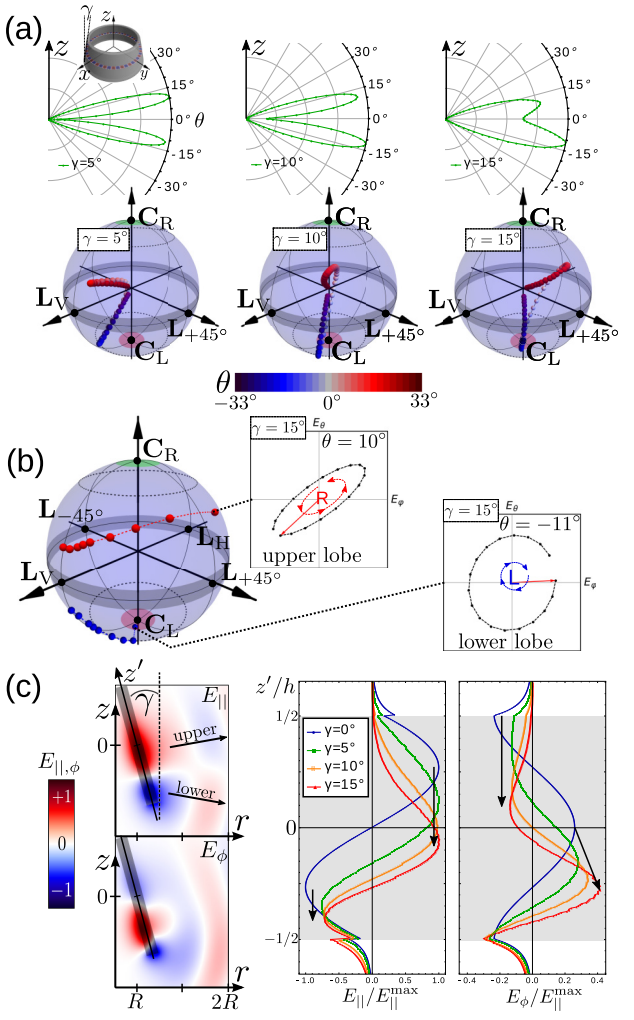

FIG. 4. Polarization states in conelike 3D-ring cavities. (a) Polar plots of far-field intensity and polarization evolution for $q = 2$ modes. (b) Polarization states at intensity maxima of the upper and lower lobes for different inclination angles $\gamma = 0°, 2°, 4°, 5°.6°, 8°, 10°, 12°, 15°$. (c) Examples for electric field distributions inside ring resonators with inclination angles $\gamma = 0°, 5°, 10°, 15°$; the left panels are for $\gamma = 15°$.

this behavior is crucial for all applications where the far field is taken as the sensing signal.

In the following, we will study this key question focusing on $q = 2$ modes. The upper row in Fig. 4(a) shows the polar far-field plots for three inclination angles $\gamma = 5°, 10°, 15°$. The lower row shows the corresponding Poincaré spheres of polarization displaying all observable polarization states when scanning the far field through the color-encoded θ range from $\theta_{\min} = -33°$ to $\theta_{\max} = +33°$.

A small wall inclination of $\gamma = 5°$ causes a rather slight asymmetry in the maximum intensity of the lobes while the shape of the far-field lobes is maintained and polarization orientation is only a slightly tilted (shifted along the equator of the Poincaré) sphere [cf. Fig. 3(b)]. However, for higher inclination angles the far-field intensity and the shape of the polarization evolution change strongly in terms of both visible asymmetries in the far-field lobes and evolution on the Poincaré sphere.

Figure 4(b) shows the Poincaré sphere of the polarization states at the far-field intensity maxima for different inclination angles γ between 0° and 15°. The red (blue) dots correspond to the upper (lower) lobes. The points right above and below $\mathbf{L}_V$ correspond to $\gamma = 0°$. Via points at $\gamma = 2°, 4°, 5°, 6°, 8°, 10°, 12°$, the end point at $\gamma = 15°$, indicated by the polarization ellipse insets, is reached. Interestingly, the upper and lower lobes experience a different polarization evolution. The polarization states of the upper lobe remain elliptically polarized but experience a strong orientation tilt. In contrast, the polarization states of the lower lobe evolve from slightly elliptical to left-hand circular polarization.

The tilt of the polarization orientation can be explained and deduced from the vector diffraction model introduced in Eq. (11), where we treat the wall of the resonator as an aperture that diffracts the waves inside the resonator into the far field. (See Appendix B 2 for more details and derivation of the following formulas.) The far-field components E_φ and E_θ in the case of conelike 3D ring cavities can be written as

$$E_\varphi = \cos(\gamma) E_{\varphi,\mathrm{ring}} + i \sin(\gamma) E_{\varphi,\mathrm{prec}}, \tag{16}$$

$$E_\theta = \cos(\gamma) E_{\theta,\mathrm{ring}} + i \sin(\gamma) E_{\theta,\mathrm{prec}}, \tag{17}$$

where $E_{\varphi,\mathrm{ring}}$ and $E_{\theta,\mathrm{ring}}$ represent the far-field components that arise from the diffraction of a 3D-ring structure [cf. Eqs. (B29) and (B30)]. The additional terms that include $E_{\varphi,\mathrm{prec}}$ and $E_{\theta,\mathrm{prec}}$ exist only for $|\gamma| > 0$ (conical cavities) and arise from the precession of the electric field along its trajectory around the cone axis [cf. Eq. (B28)]. The precession terms are phase shifted by $\pi/2$ with respect to the ring diffraction terms as indicated by the prefactor i. As a consequence, both components E_φ and E_θ undergo a phase change which increases with increasing inclination angle γ. This is the very origin of the phase δ between the far-field components E_φ and E_θ, which in turn results in a change of the orientation angle Ψ [cf. Eq. (8)]. This explains the general feature of the increasing tilt angle Ψ with increasing inclination angle γ as shown in Fig. 4(b).

The different evolution of the upper and lower lobes can be explained by an asymmetric distortion of the amplitudes. By inclining the resonator wall, the mirror symmetry at the $z = 0$ plane is broken. Thus, we expect that the electric field amplitudes $\tilde{A}_\parallel(u')$ and $\tilde{A}_\phi(u')$ inside the resonator wall undergo a distortion. The left panels of Fig. 4(c) show an example of such a distorted electric field. The panels on the right-hand side of Fig. 4(c) display a comparison of $E_\parallel$ and E_ϕ at four different inclination angles γ, where $E_\parallel$ and E_ϕ correspond to the field distribution along the z' axis (at half wall thickness) and the longitudinal E_ϕ component as indicated in the panels on the left-hand side.

First of all, we notice that the entire distributions of $E_\parallel$ and E_ϕ shift more towards the broader end of the cone (into the $-z'$ direction) with increasing γ. Using the graph of $E_\parallel$ at $\gamma = 15°$ as an example, we see that (i) $E_\parallel$ for $z' > 0$ decays to zero inside the cavity and (ii) the distance between the maximum and minimum is reduced compared to $\gamma = 0°$. These facts indicate that the confinement length scale along the height of the

resonator wall is reduced. As a result, the longitudinal component E_ϕ increases because of $E_\phi \propto \partial E_\parallel/\partial z'$. The increase of E_ϕ at $\gamma = 15^\circ$ is noticeable through the increase of the height of the central maximum as indicated by the black arrow. Thus, the overall spin-orbit interaction is enhanced and explains the generally increasing ellipticity χ with increasing γ.

Concerning the lobe asymmetry, we use again the graph of $E_\parallel$ at $\gamma = 15^\circ$ as an example. We see that the maximum ($z' > 0$) shifts by a larger distance than the minimum ($z' < 0$), as indicated by the black arrows. As a result, the upper part of the distribution is stretched while the lower part is compressed (asymmetric distortion). The stretching extends the confinement length scale locally and therefore the spin-orbit coupling is reduced within this length scale. On the other hand, the compression reduces the confinement length scale locally and therefore the spin-orbit coupling is enhanced within this length scale. This allows us to qualitatively explain the behavior of the far-field polarization states of the two different lobes shown in Fig. 4(b). As a result, the lower far-field lobes (blue points) emerging from the lower part of the distorted field distribution show an increased ellipticity with respect to the upper far-field lobes (red points) that emerge from the upper part of the distorted field distribution.

The property of asymmetrical distortion of the amplitudes is linked to the far-field components E_φ and E_θ via the diffraction integral. We exemplarily show this for $E_{\varphi,\mathrm{ring}}$. According to the derivations in Appendix B [cf. Eq. (B29)], $E_{\varphi,\mathrm{ring}}$ is given by

$$E_{\varphi,\mathrm{ring}} = [K_{\mathrm{x,ring}}\cos(\varphi) + K_{\mathrm{y,ring}}\sin\varphi]\sin(\theta) - K_{\mathrm{z,ring}}\cos\theta, \tag{18}$$

where $K_{\mathrm{x,ring}}$, $K_{\mathrm{y,ring}}$, and $K_{\mathrm{z,ring}}$ are the components of the ring diffraction integral. For example, $K_{\mathrm{x,ring}}$ is given by

$$K_{\mathrm{x,ring}} = hR\int_{-1/2}^{1/2}\cos(\gamma)\tilde{A}_\parallel(u')F_\mathrm{x}(u')\exp[-i\cos(\gamma)\tilde{k}_2u']du', \tag{19}$$

where $F_\mathrm{x}(u')$ is a function resulting from the ϕ' integration [cf. Eq. (B40)]. Note that the u' integration cannot be treated approximately as a mere Fourier transform of the amplitudes as in the case of the 3D ring [cf. Eq. (14)].

We point out that Eqs. (16) and (17) provide a formula which takes the effects of diffraction and precession of the electric field into account. These effects determine the orientation angle Ψ and the ellipticity χ [cf. Eqs. (8) and (9)]. Especially important is that Ψ, χ, and the handedness σ depend on the far-field observation direction, which is described by the angles φ and θ. We would like to highlight that the quantities Ψ and χ are observable in the far field, but the WGM inside the resonator wall has a different and complicated polarization state. The connection between the polarization state of the WGM and the observable far-field quantities Ψ and χ is provided by diffraction and precession.

In [15], an inclination of the far-field polarization orientation and an increase of the ellipticity were experimentally observed for inhomogeneous anisotropic conelike cavities and explained in terms of noncyclic geometric phases. Here we find a similar behavior in the generic case of homogeneous isotropic cavities and an explanation in terms of diffraction theory.

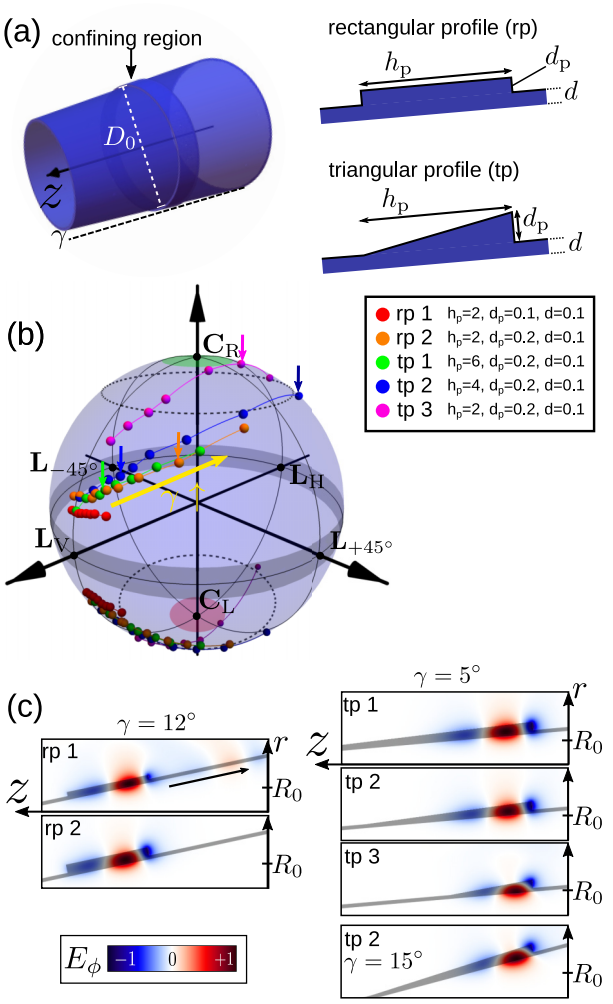

FIG. 5. Geometry and polarization states of conelike tube cavities. (a) Illustration of the geometry of the tube cavity and different confinement profiles of the confining region. (b) Polarization states at a maximum far-field intensity of $q = 2$ modes of different confinement profiles. The parameters displayed in the legend are given in microns. (c) Comparison of field distributions E_ϕ at different profile configurations and inclination angles. See the text for details.

V. COMPLEX CONELIKE TUBULAR CAVITIES

We have seen in the previous sections that the spin-orbit interaction of light depends sensitively on the confinement of light that is determined by both the resonator geometry and the specific resonance pattern. To further illustrate this intricate interplay, we will now study complex, composite 3D conelike tubular cavities where the confining region of the cavity is extended by an additional layer of cavity material [see Fig. 5(a)]. This resonator wall geometry is inspired by rolled-up cones where regions of different wall thicknesses emerge (e.g., cf. [11,15,44]) and by cavities where an extra layer of material results from an etching process (cf. [14]).

The confining region is realized by two different axial profiles, a rectangular profile (rp) and triangular profile (tp),

as shown on the right-hand side of Fig. 5(a). We consider conelike cavities with a mean diameter $D_0 = 6\ \mu$m and total height $h_T = 20\ \mu$m. We will investigate the far-field polarization states and how they depend on (i) the confining profile and (ii) the inclination angle γ of the tube wall. The results are shown in Fig. 5(b). The far-field polarization states of maximum intensity of $q = 2$ modes confined in five different axial profiles are shown on the Poincaré sphere with its upper (lower) hemisphere corresponding to the upper (lower) lobes. The yellow arrow indicates the generic polarization evolution for increasing inclination angle γ (again, with the data points closest to the longitude of $\mathbf{L}_V$ corresponding to $\gamma = 0^\circ$). We observe the general feature that with increasing γ the polarization states evolve into the direction of $\mathbf{L}_{+45^\circ}$ while getting closer to the poles of the sphere. In other words, orientation tilt Ψ and the ellipticity χ increase with increasing wall inclination. This behavior is very similar to the one observed before [cf. Fig. 4(b)]. The evolution of the polarization state depends on the confining profile that in turn controls the mode's axial field distribution, and hence, following Eq. (5), the spin-orbit interaction. In the case of the rectangular profile, the far-field polarization states depend strongly on the thickness of the profile d_p as represented by the red (rp 1) and orange (rp 2) data points on the Poincaré sphere in Fig. 5(b). The inclination angles of the rectangular profile 1 range from $\gamma_{min} = 0^\circ$ up to $\gamma_{max} = 8^\circ$ in steps of 1°. For angles higher than γ_{max} the modes become unstable and propagate down (towards the broader end of) the cone because the confining profile is too thin to stably host a WGM resonance. This finding is illustrated on the left-hand side of Fig. 5(c). The upper (lower) image shows a section around the confining region rp 1 (rp 2) for $\gamma = 12^\circ$, overlaid with the electric field component E_ϕ obtained from FDTD simulations. We clearly see that a wave packet is leaving the profile rp 1 and propagating towards the broader part of the cone (black arrow). This indicates an unstable mode and no stationary far-field polarization states can be found. Contrary to this, the thicker profile rp 2 ensures the existence of a stable WGM-type resonance [see the lower left panel in Fig. 5(c), which corresponds to the state marked by an orange arrow on the Poincaré sphere in Fig. 5(b)].

The upper three images on the right-hand side of Fig. 5(c) compare the electric field distribution E_ϕ at different configurations of the triangular profile tp 1, tp 2, and tp 3 but all at constant wall inclination angle $\gamma = 5^\circ$. The corresponding far-field polarization states are marked by green (tp 1), blue (tp 2), and magenta (tp 3) arrows on the Poincaré sphere of Fig. 5(b). We see that the difference between the field distribution in tp 1 and tp 2 is small. As a consequence, the corresponding far-field polarization states are located in close proximity on the Poincaré sphere [cf. Fig. 5(b)]. The highlighted polarization state corresponding to tp 2 shows a slightly higher tilt and ellipticity because the profile tp 2 provides stronger confinement, and hence stronger spin-orbit interaction due to the reduced profile height h_p.

On the other hand, the difference between the field distributions in tp 2 and tp 3 is more pronounced due to the further reduced profile height of tp 3. The E_ϕ distribution is now visibly characterized by a strong mode distortion that causes a higher spin-orbit interaction. As a result, the corresponding far-field polarization state of tp 3 [highlighted by the magenta arrow on the Poincaré sphere in Fig. 5(b)] is almost circularly polarized.

For comparison, the lowest panel on the right-hand side of Fig. 5(c) shows the E_ϕ distribution of tp 2 at the higher inclination angle of $\gamma = 15^\circ$. Interestingly, this E_ϕ distribution is very similar to that of tp 3 because it displays a similar distortion (cf. the red areas of the E_ϕ distributions). We conclude that the high inclination angle of $\gamma = 15^\circ$ of tp 2 results in a comparable confinement and distortion of the mode as caused by the profile tp 3 at lower angle. As a result, the corresponding far-field polarization states display similar features indicated by the dark blue and magenta arrows on the Poincaré sphere.

The overall increasing tilt of the polarization orientation and ellipticity caused by the triangular profiles result from a enhanced precession of the electric field and a stronger spin-orbit coupling, respectively. The stronger spin-orbit coupling can be explained by an increased axial confinement. The enhanced precession of the electric field can be explained by an increased effective inclination angle γ_{eff}. In addition to the inclined cone wall described by γ, the triangular profile provides a further local inclination given by $\tan\gamma_p = d_p/h_p$. The interplay of both inclinations leads to $\gamma_{eff} > \gamma$ and thus, according to the introduced diffraction model, an increased inclination angle leads to an increased tilt of the polarization orientation.

VI. SUMMARY

We have performed FDTD simulations in order to investigate the spin-orbit coupling of light in three-dimensional cylindrical and tubelike whispering gallery mode resonators. We have shown that the spin-orbit interaction in cylindrical ring cavities results in elliptical far-field polarization and spatial separation of left and right elliptically polarized light in the far field but without tilting of the orientation angle. The ellipticity and spatial polarization separation of the far field is more pronounced in axially higher excited whispering gallery modes due to increased spin-orbit coupling.

Furthermore, we have shown that the inclination of the resonator wall realized by cylindrical ringlike cone cavities enhances the ellipticity of the far field further and induces a tilt of the far-field polarization orientation even for homogeneous and isotropic material systems. The enhancement of the far-field ellipticity arises from the asymmetric distortion of the electric field distribution at the resonator wall. This asymmetric distortion causes different elliptical polarization states of upper and lower far-field lobes. The tilt of the polarization orientation arises from the precession of the electric field vector along its trajectory around the cone axis. The connection between the local polarization state of the whispering gallery mode inside the resonator and the observable far-field quantities Ψ and χ is provided by the introduced diffraction model. We emphasize that the polarization orientation Ψ, the ellipticity χ and the handedness σ depend on the direction of observation described by the far-field angles φ and θ.

In the end, we have investigated complex conelike tubular cavities with different confining profiles. Similar to the case of ringlike cone cavities, the tilt of the polarization orientation Ψ

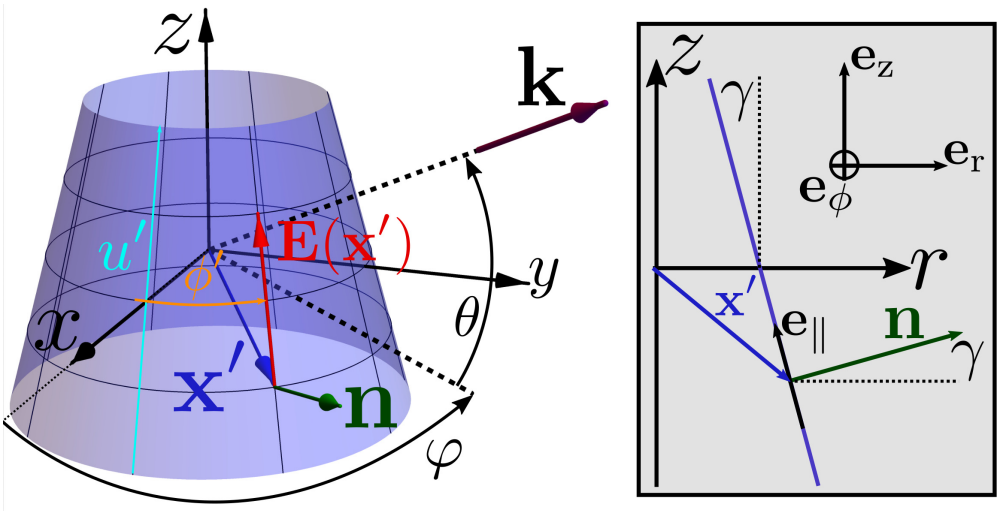

FIG. 6. Illustration of the geometry. The blue cone surface is parametrized by (u', ϕ'), θ and φ are the far-field angles, and γ is the angle between the cone surface and the z axis.

and the ellipticity χ increase with increasing wall inclination γ. Furthermore, we have discovered that a triangular profile enhances the tilt of the orientation and the ellipticity because of an increased effective inclination γ_{eff} and a stronger spin-orbit coupling, respectively.

Our results demonstrate the importance and variety of spin-orbit coupling of light in three-dimensional whispering gallery mode resonators as a fundamental effect and may be important for optical information technology or polarization-dependent sensing applications.

ACKNOWLEDGMENTS

This work was partly supported by Emmy-Noether program of the German Research Foundation.

APPENDIX A: FDTD METHOD

All data presented in this work were obtained from FDTD calculation based on the open source software package MEEP [46].

We give a short description of the procedure. In the first step, we have computed the resonance frequencies of TE-like modes for the following structures: 3D-ring cavities (cf. Sec. III), conelike ring cavities (cf. Sec. IV), and conelike tubular cavities (cf. Sec. V). In the second step, we have computed the electric field distribution of the resonances and let the fields evolve for one period in order to make 20 snapshots of the electric field in the region around the cavity (near field).

In addition to this, we computed 20 snapshots of the electric field on a circular arc with radius of $r_{\text{FF}} = 50\ \mu$m (approximately satisfying the far-field condition $r_{\text{FF}} \gg R^2/\lambda_{q=1} \approx 6\ \mu$m) within the range of $\theta = \pm 45^\circ$ in steps of $\Delta\theta = 1^\circ$. These far-field snapshots were used to calculate $|E_{\text{FF}}|^2$ (as a measure of the far-field intensity) and the orientation angle Ψ and the ellipticity angle χ of the polarization ellipse. The handedness σ was determined by the rotation sense of the electric field vector describing the polarization ellipse. Note that, due to the cylindrical symmetry of the considered structures, we have used cylindrical coordinates in MEEP. As a result, the computed fields have the form $E = f(r, z)\exp(im\phi)$ and thus they represent azimuthally propagating fields.

APPENDIX B: VECTOR DIFFRACTION THEORY

We start by recalling the definition of the electric far-field field vector according to Kirchhoff vector diffraction [42]

$$\mathbf{E}_{\text{FF}}(\varphi,\theta) \propto \mathbf{k}(\varphi,\theta) \times \iint \mathbf{n}(\mathbf{x}') \times \mathbf{E}(\mathbf{x}') e^{-i\mathbf{k}\cdot\mathbf{x}'} da' = \mathbf{k}(\varphi,\theta) \times \mathbf{K}(\varphi,\theta), \tag{B1}$$

with $\mathbf{x}' = \mathbf{x}'(u', \phi')$ the position vector pointing onto the surface S parametrized by the elevation parameter u' and the azimuthal parameter ϕ' (cf. Fig. 6). The vector $\mathbf{n}$ is the unit normal vector of the surface S, da' is the differential surface area element given by $|\frac{\partial \mathbf{x}'}{\partial u'} \times \frac{\partial \mathbf{x}'}{\partial \phi'}| du' d\phi' = s(u', \phi') du' d\phi'$, and $\mathbf{k}(\varphi, \theta)$ represents the wave vector pointing into the observation direction (φ, θ) in the far field, $\mathbf{k} = k[\cos\theta\cos(\varphi)\mathbf{e}_x + \cos\theta\sin(\varphi)\mathbf{e}_y + \sin(\theta)\mathbf{e}_z]$ (cf. Fig. 1). Thus, the scalar product $\mathbf{k} \cdot \mathbf{x}' = g(u', \phi', \theta, \varphi)$ is a function of θ, φ, u', and ϕ'.

1. Vector diffraction theory for cylindrical ring cavities ($\gamma = 0$)

First, we investigate the simple case of a cylindrical ring cavity with $\gamma = 0$, that is, the wall of the ring cavity is aligned parallel to the z axis [cf. Fig. 2(a)].

The position vector can be written as $\mathbf{x}'_{\mathrm{ring}}(u', \phi') = R\mathbf{e}_{\mathrm{r}}(\phi') + hu'\mathbf{e}_{\mathrm{z}}$, where $\mathbf{e}_{\mathrm{r}}$ (pointing away radially from the z axis) and $\mathbf{e}_{\mathrm{z}}$ (pointing parallel to the z axis) are unit vectors of cylindrical coordinates (cf. the inset of Fig. 6). The parameter u' ranges from $-\frac{1}{2}$ to $\frac{1}{2}$ and ϕ' ranges from 0 to 2π. The normal vector of S coincides with $\mathbf{e}_{\mathrm{r}}$, $\mathbf{n} = \mathbf{e}_{\mathrm{r}}$. The electric fields at the cylindrical diffracting surface can be represented as $\mathbf{E}(\mathbf{x}'_{\mathrm{ring}}) = [A_{\mathrm{z}}(z')\mathbf{e}_{\mathrm{z}} + A_{\phi}(z')\mathbf{e}_{\phi}]\exp(im\phi') = [\tilde{A}_{\mathrm{z}}(u')\mathbf{e}_{\mathrm{z}} + \tilde{A}_{\phi}(u')\mathbf{e}_{\phi}]\exp(im\phi')$. Thus, the term $\mathbf{n}(\mathbf{x}'_{\mathrm{ring}}) \times \mathbf{E}(\mathbf{x}'_{\mathrm{ring}})$ becomes

$$\mathbf{n}(\mathbf{x}'_{\mathrm{ring}}) \times \mathbf{E}(\mathbf{x}'_{\mathrm{ring}}) = \mathbf{e}_{\mathrm{r}}(\phi') \times \mathbf{E}(u', \phi') = [\tilde{A}_{\phi}(u')\mathbf{e}_{\mathrm{z}} - \tilde{A}_{\mathrm{z}}(u')\mathbf{e}_{\phi}(\phi')]\exp(im\phi'). \tag{B2}$$

The scalar product $\mathbf{k} \cdot \mathbf{x}'_{\mathrm{ring}}$ separates into two terms depending on ϕ' and u', respectively:

$$\mathbf{k} \cdot \mathbf{x}'_{\mathrm{ring}} = kR\cos\theta\cos(\phi' - \varphi) + kh\sin(\theta)u' = \tilde{k}_1\cos(\phi' - \phi) + \tilde{k}_2 u'. \tag{B3}$$

In the following, we will evaluate the components K_{x}, K_{y}, and K_{z} of the diffraction integral $\mathbf{K}$,

$$K_{\mathrm{x}} = hR\int_0^{2\pi} \sin\phi' \exp(im\phi')\exp[-i\tilde{k}_1\cos(\phi' - \varphi)]d\phi' \int_{-1/2}^{1/2} \tilde{A}_{\mathrm{z}}(u')\exp(-i\tilde{k}_2 u')du' \tag{B4}$$

$$= hR\hat{\Phi}_{\mathrm{s}}(\tilde{k}_1, \varphi)\hat{A}_{\mathrm{z}}(\tilde{k}_2), \tag{B5}$$

$$K_{\mathrm{y}} = -hR\int_0^{2\pi} \cos\phi' \exp(im\phi')\exp[-i\tilde{k}_1\cos(\phi' - \varphi)]d\phi' \int_{-1/2}^{1/2} \tilde{A}_{\mathrm{z}}(u')\exp(-i\tilde{k}_2 u')du' \tag{B6}$$

$$= -hR\hat{\Phi}_{\mathrm{c}}(\tilde{k}_1, \varphi)\hat{A}_{\mathrm{z}}(\tilde{k}_2), \tag{B7}$$

$$K_{\mathrm{z}} = hR\int_0^{2\pi} \exp(im\phi')\exp[-i\tilde{k}_1\cos(\phi' - \varphi)]d\phi' \int_{-1/2}^{1/2} \tilde{A}_{\phi}(u')\exp(-i\tilde{k}_2 u')du' \tag{B8}$$

$$= i\frac{R^2}{m}\int_0^{2\pi} \exp(im\phi')\exp[-i\tilde{k}_1\cos(\phi' - \varphi)]d\phi' \int_{-1/2}^{1/2} \frac{\partial\tilde{A}_{\mathrm{z}}(u')}{\partial u'}\exp(-i\tilde{k}_2 u')du' \tag{B9}$$

$$= \frac{R^2}{m}\hat{\Phi}_1(\tilde{k}_1, \varphi)[-\tilde{k}_2\hat{A}_{\mathrm{z}}(\tilde{k}_2) + i\tilde{A}_{\mathrm{z}}(u')\exp(-i\tilde{k}_2 u')|_{u'_1=-1/2}^{u'_2=1/2}], \tag{B10}$$

where we used $A_{\phi}(z') = i(R/m)[\partial A_{\mathrm{z}}(z')/\partial z']$ and therefore $\tilde{A}_{\phi}(u') = i(R/mh)[\partial\tilde{A}_{\mathrm{z}}(u')/\partial u']$ and integrated by parts.

In the next step, we simplify the $\hat{\Phi}_{\mathrm{s}}(\tilde{k}_1, \varphi)$, $\hat{\Phi}_{\mathrm{c}}(\tilde{k}_1, \varphi)$, and $\hat{\Phi}_1(\tilde{k}_1, \varphi)$ using the substitution $\phi' = \phi + \varphi$ and taking advantage of angle sum identities of sine and cosine,

$$\hat{\Phi}_{\mathrm{s}}(\tilde{k}_1, \varphi) = \exp(im\varphi)[\cos(\varphi)I_{\mathrm{s}} + \sin(\varphi)I_{\mathrm{c}}], \tag{B11}$$

$$\hat{\Phi}_{\mathrm{c}}(\tilde{k}_1, \varphi) = \exp(im\varphi)[\cos(\varphi)I_{\mathrm{c}} - \sin(\varphi)I_{\mathrm{s}}], \tag{B12}$$

$$\hat{\Phi}_1(\tilde{k}_1, \varphi) = \exp(im\varphi)I_1, \tag{B13}$$

where the I_{s}, I_{c}, and I_1 are given by

$$I_{\mathrm{s}} = \int_0^{2\pi} \sin\phi\exp(im\phi)\exp(-i\tilde{k}_1\cos\phi)d\phi = -\exp\left(-i\frac{\pi}{2}m\right)\frac{m}{\tilde{k}_1}J_m(\tilde{k}_1), \tag{B14}$$

$$I_{\mathrm{c}} = \int_0^{2\pi} \cos\phi\exp(im\phi)\exp(-i\tilde{k}_1\cos\phi)d\phi = \exp\left(-i\frac{\pi}{2}(m+1)\right)\frac{J_{m+1}(\tilde{k}_1) - J_{m-1}(\tilde{k}_1)}{2}, \tag{B15}$$

$$I_1 = \int_0^{2\pi} \exp(im\phi)\exp(-i\tilde{k}_1\cos\phi)d\phi = \exp\left(-i\frac{\pi}{2}m\right)J_m(\tilde{k}_1). \tag{B16}$$

The integrals I_{s}, I_{c}, and I_1 were evaluated using the Jacobi-Anger expansion [47]

$$\exp(iz\cos\phi) = \sum_{n=-\infty}^{+\infty} \exp\left(i\frac{\pi}{2}n\right)J_n(z)\exp(in\phi), \tag{B17}$$

where J_n is the Bessel function of the first kind. Now we derive the far-field components E_{φ} and E_{θ},

$$E_{\varphi} = \mathbf{E}_{\mathrm{FF}} \cdot \mathbf{e}_{\varphi} = (\mathbf{k} \times \mathbf{K}) \cdot \mathbf{e}_{\varphi} = -\mathbf{K} \cdot \mathbf{e}_{\theta} = (K_{\mathrm{x}}\cos\varphi + K_{\mathrm{y}}\sin\varphi)\sin\theta - K_{\mathrm{z}}\cos\theta$$

$$= hR\exp(im\varphi)\exp\left(-i\frac{\pi}{2}m\right)J_m(\tilde{k}_1)\left(\hat{A}_{\mathrm{z}}(\tilde{k}_2)\frac{\tilde{k}_1^2 - m^2}{m\tilde{k}_1}\sin\theta - \Delta\cos\theta\right), \tag{B18}$$

$$E_\theta = \mathbf{E}_{\mathrm{FF}} \cdot \mathbf{e}_\theta = (\mathbf{k} \times \mathbf{K}) \cdot \mathbf{e}_\theta = \mathbf{K} \cdot \mathbf{e}_\varphi = -K_{\mathrm{x}} \sin\varphi + K_{\mathrm{y}} \cos\varphi$$
$$= hR \exp(im\varphi) \exp\left(-i\frac{\pi}{2}(m+1)\right) \frac{J_{m-1}(\tilde{k}_1) - J_{m+1}(\tilde{k}_1)}{2} \hat{A}_{\mathrm{z}}(\tilde{k}_2), \tag{B19}$$

where Δ represents the boundary contributions

$$\Delta = \frac{i}{m}\frac{R}{h}\tilde{A}_{\mathrm{z}}(u') \exp(-i\tilde{k}_2 u') \Big|_{u'_1=-1/2}^{u'_2=1/2} \tag{B20}$$
$$= \frac{2R}{mh}\tilde{A}_{\mathrm{z}}(\tfrac{1}{2}) \times \begin{cases} \sin(\tilde{k}_2/2) & \text{for } q = 1, 3, 5, \ldots \\ i\cos(\tilde{k}_2/2) & \text{for } q = 2, 4, 6, \ldots . \end{cases} \tag{B21}$$

2. Vector diffraction theory for conelike ring and tubular cavities ($\gamma > 0$)

In this section, we investigate the more complicated situation of an inclined cavity wall, that is, $\gamma > 0$.

The normal vector $\mathbf{n}$ of the surface S representing a thin-walled conical cavity can be written as

$$\mathbf{n} = \cos(\gamma)\mathbf{e}_{\mathrm{r}} + \sin(\gamma)\mathbf{e}_{\mathrm{z}}, \tag{B22}$$

where γ is the angle between the cone's surface and the z axis or the half opening angle of the cone. Thus, the term $\mathbf{n} \times \mathbf{E}$ becomes

$$\mathbf{n} \times \mathbf{E} = \cos(\gamma)\mathbf{e}_{\mathrm{r}} \times \mathbf{E} + \sin(\gamma)\mathbf{e}_{\mathrm{z}} \times \mathbf{E} \tag{B23}$$
$$= \cos(\gamma)\mathbf{e}_{\mathrm{r}} \times \mathbf{E} + \sin\gamma \left(-im\mathbf{E} + \frac{\partial \mathbf{E}}{\partial \phi'}\right). \tag{B24}$$

Here we took advantage of the fact that the WGM is propagating on a circular trajectory around the cone (or z) axis. As a consequence, the triad of its moving frame is precessing around the z axis. The direction vectors of the triad of the moving frame coincide (locally) with the direction vectors of cylindrical coordinates. The change of the electric field vector along its path around the axis of the cone can be written as

$$\frac{\partial \mathbf{E}}{\partial \phi'} = im\mathbf{E} + \sum_{j=r,\phi,z} E_j \frac{\partial \mathbf{e}_j}{\partial \phi'} = im\mathbf{E} + \mathbf{e}_{\mathrm{z}} \times \mathbf{E}, \tag{B25}$$

where the change of the unit direction vectors $\frac{\partial \mathbf{e}_j}{\partial \phi'}$ represents the precession of the triad around the z axis and therefore is equal to $\mathbf{e}_{\mathrm{z}} \times \mathbf{E}$.

Inserting this into the definition of the electric far-field vector, we obtain

$$\mathbf{E}_{\mathrm{FF}} = \mathbf{k} \times \left[\cos\gamma \iint \mathbf{e}_{\mathrm{r}} \times \mathbf{E}\, e^{-i\mathbf{k}\cdot\mathbf{x}'} da' + \sin\gamma \iint \left(-im\mathbf{E} + \frac{\partial \mathbf{E}}{\partial \phi'}\right) e^{-i\mathbf{k}\cdot\mathbf{x}'} da'\right]. \tag{B26}$$

The integration over the cone area $da' = s(u', \phi')du'd\phi'$ can be interpreted to be comprised of (i) an integration along the trajectory of the WGM represented by the $\int(\cdots)d\phi'$ integral and (ii) an integration perpendicular to the trajectory (along the height of the cavity) represented by the $\int(\cdots)du'$ integral.

In the second term on the right-hand side we can integrate by parts the $\int(\cdots)d\phi'$ integral

$$\iint \frac{\partial \mathbf{E}}{\partial \phi'} e^{-i\mathbf{k}\cdot\mathbf{x}'} da' = \int \mathbf{E}(u', \phi')\, e^{-i\mathbf{k}\cdot\mathbf{x}'} s(u', \phi') \Big|_{\phi'=0}^{\phi'=2\pi} du' - \iint \left(-i\mathbf{k} \cdot \frac{\partial \mathbf{x}'}{\partial \phi'} + \frac{1}{s}\frac{\partial s}{\partial \phi'}\right)\mathbf{E}\, e^{-i\mathbf{k}\cdot\mathbf{x}'} da'. \tag{B27}$$

Note that the last term inside the integral on the right-hand side vanishes for cylindrical symmetry, $\partial s/\partial\phi' = 0$. The first term depends on the electric field of the start ($\phi' = 0$) and end ($\phi' = 2\pi$) points of the trajectory around the cone axis. In the case of a WGM as a cyclical stationary phenomenon, this difference vanishes because the electric field at the start and the end is the same or phase shifted by integer multiples of 2π (constructive interference condition). However, this term may contribute in more complex, noncyclical wave dynamics.

Finally, the electric far-field vector can be written as

$$\mathbf{E}_{\mathrm{FF}}(\theta, \varphi) = \mathbf{k}(\theta, \varphi) \times \mathbf{K}(\varphi, \theta)$$
$$= \mathbf{k}(\theta, \varphi) \times \left[\cos(\gamma) \iint \mathbf{e}_{\mathrm{r}} \times \mathbf{E}(u', \phi')\, e^{-i\mathbf{k}\cdot\mathbf{x}'} da' \; - \; i\sin(\gamma) \iint \left(m - \mathbf{k} \cdot \frac{\partial \mathbf{x}'}{\partial \phi'}\right)\mathbf{E}(u', \phi')\, e^{-i\mathbf{k}\cdot\mathbf{x}'} da'\right]$$
$$= \mathbf{k}(\theta, \varphi) \times \left(\cos(\gamma)\mathbf{K}_{\mathrm{ring}}(\varphi, \theta) - i\sin(\gamma)\mathbf{K}_{\mathrm{prec}}(\varphi, \theta)\right). \tag{B28}$$

We notice that the first term on the right-hand side resembles the vector diffraction of a 3D ring multiplied by $\cos\gamma$ [cf. Eq. (B2)]. The additional second term on the right-hand side exists only for $\gamma > 0$ (conical cavities) and arises from the precession of the electric field along its trajectory around the cone axis. This term is phase shifted by $\pi/2$ with respect to the first term, as indicated by the prefactor i. The above-mentioned reasoning resembles, in a number of aspects, the action of geometric phases known in various examples throughout mesoscopic physics of electrons and photons and beyond [48]. In particular, we find the cone's opening angle 2γ to play an important role, as expected, for example, from electronic transport in inhomogeneous magnetic fields [38–41]. In idealized one-dimensional electronic magnetotransport the geometric phase is known to be directly related to the cone's opening angle [more precisely, it is half (for electronic spin) of the solid angle spanned by the spin dynamics in parameter (magnetic field) space as the ring trajectory is traversed]. However, Eq. (B28) proves things to be more complex in the generic (and three-dimensional) situation considered here, where in particular an additional transition to the far field has to be taken into account.

In the same fashion as in Sec. 1, we derive the far-field components E_φ and E_θ,

$$\begin{aligned} E_\varphi = -\mathbf{K}\cdot\mathbf{e}_\theta &= \cos\gamma\{[K_{\mathrm{x,ring}}\cos(\varphi) + K_{\mathrm{y,ring}}\sin\varphi]\sin(\theta) - K_{\mathrm{z,ring}}\cos\theta\} \\ &\quad + i\sin\gamma[(K_{\mathrm{x,prec}}\cos\varphi + K_{\mathrm{y,prec}}\sin\varphi)\sin\theta - K_{\mathrm{z,prec}}\cos\theta] \\ &= \cos(\gamma)E_{\varphi,\mathrm{ring}} + i\sin(\gamma)E_{\varphi,\mathrm{prec}}, \end{aligned} \tag{B29}$$

$$\begin{aligned} E_\theta = \mathbf{K}\cdot\mathbf{e}_\varphi &= \cos\gamma(-K_{\mathrm{x,ring}}\sin\varphi + K_{\mathrm{y,ring}}\cos\varphi) + i\sin\gamma(-K_{\mathrm{x,prec}}\sin\varphi + K_{\mathrm{y,prec}}\cos\varphi) \\ &= \cos(\gamma)E_{\theta,\mathrm{ring}} + i\sin(\gamma)E_{\theta,\mathrm{prec}}. \end{aligned} \tag{B30}$$

Notice that both components E_φ and E_θ undergo a phase shift that arises from the precession of the electric field vector inside the conical cavity. This is the very origin of the phase δ between the far-field components E_φ and E_θ, which in turn results in a change of the orientation angle Ψ [cf. Eq. (8)].

For the sake of completeness, we examine the components of the diffraction integral in Eq. (B28). To this end, we express the electric field vector of the TE-like WGM by the unit vector parallel to the cone surface and by the azimuthal unit vector $\mathbf{E}(u',\phi') = [\tilde{A}_\parallel(u')\mathbf{e}_\parallel(\phi') + \tilde{A}_\phi(u')\mathbf{e}_\phi(\phi')]\exp(im\phi')$ with $\mathbf{e}_\parallel = -\sin(\gamma)\mathbf{e}_\mathrm{r} + \cos(\gamma)\mathbf{e}_\mathrm{z}$ (cf. Fig. 6). Thus, the components of $\mathbf{K}_{\mathrm{ring}}$ and $\mathbf{K}_{\mathrm{prec}}$ can be written as

$$K_{\mathrm{x,ring}} = \iint \cos(\gamma)\tilde{A}_\parallel(u')\sin\phi'\exp(im\phi')\exp(-i\mathbf{k}\cdot\mathbf{x}')da', \tag{B31}$$

$$K_{\mathrm{y,ring}} = -\iint \cos(\gamma)\tilde{A}_\parallel(u')\cos\phi'\exp(im\phi')\exp(-i\mathbf{k}\cdot\mathbf{x}')da', \tag{B32}$$

$$K_{\mathrm{z,ring}} = \iint \tilde{A}_\phi(u')\exp(im\phi')\exp(-i\mathbf{k}\cdot\mathbf{x}')da', \tag{B33}$$

$$K_{\mathrm{x,prec}} = \iint \tilde{m}[\sin(\gamma)\tilde{A}_\parallel(u')\cos(\phi') + \tilde{A}_\phi(u')\sin\phi']\exp(im\phi')\exp(-i\mathbf{k}\cdot\mathbf{x}')da', \tag{B34}$$

$$K_{\mathrm{y,prec}} = \iint \tilde{m}[\sin(\gamma)\tilde{A}_\parallel(u')\sin(\phi') - \tilde{A}_\phi(u')\cos\phi']\exp(im\phi')\exp(-i\mathbf{k}\cdot\mathbf{x}')da', \tag{B35}$$

$$K_{\mathrm{z,prec}} = -\iint \tilde{m}\cos(\gamma)\tilde{A}_\parallel(u')\exp(im\phi')\exp(-i\mathbf{k}\cdot\mathbf{x}')da', \tag{B36}$$

where $\tilde{m} = m - \mathbf{k}\cdot\frac{\partial\mathbf{x}'}{\partial\phi'} = m - k(R - u'h\sin\gamma)\sin(\phi'-\varphi)\cos\theta$.

The parametrization $\mathbf{x}'$ of the surface S representing the inclined cone surface reads

$$\begin{aligned} \mathbf{x}'(\phi',u') &= R\mathbf{e}_\mathrm{r}(\phi') + u'h\mathbf{e}_\parallel(\phi') = R\mathbf{e}_\mathrm{r}(\phi') + u'h\cos(\gamma)\mathbf{e}_\mathrm{z} - u'h\sin(\gamma)\mathbf{e}_\mathrm{r} \\ &= (R - u'h\sin\gamma)\mathbf{e}_\mathrm{r} + u'h\cos(\gamma)\mathbf{e}_\mathrm{z}. \end{aligned} \tag{B37}$$

Evaluating the term $\mathbf{k}\cdot\mathbf{x}'$ yields thus

$$\begin{aligned} \mathbf{k}\cdot\mathbf{x}' &= k(R - u'h\sin\gamma)(\cos\theta\cos\varphi\cos\phi' + \cos\theta\sin\varphi\sin\phi') + u'hk\cos\gamma\sin\theta \\ &= \tilde{k}_1\cos(\phi'-\varphi) + \cos(\gamma)\tilde{k}_2u' - \sin(\gamma)kh\cos\theta\cos(\phi'-\varphi)u', \end{aligned} \tag{B38}$$

where the additional third term on the right-hand side arises from the inclination of the wall [cf. Eq. (B3)] and depends on ϕ' and u'. As a result, the components of the diffraction formula do not factorize into a ϕ' and u' integration as in the case of the 3D ring. Note that the u' integrations cannot be treated approximately as a mere Fourier transform of the amplitudes as in the case of the 3D ring. We demonstrate this exemplarily for $K_{\mathrm{x,ring}}$,

$$K_{\mathrm{x,ring}} = hR\int_{-1/2}^{1/2}\cos(\gamma)\tilde{A}_\parallel(u')F_\mathrm{x}(u')\exp[-i\cos(\gamma)\tilde{k}_2u']du', \tag{B39}$$

$$F_x(u') = s(u') \int_0^{2\pi} \sin\phi' \exp(im\phi') \exp\{-i[\tilde{k}_1 - \sin(\gamma) kh \cos(\theta) u'] \cos(\phi' - \varphi)\} d\phi', \tag{B40}$$

where $s(u') = 1 - u' \frac{h}{R} \sin\gamma$. We discover a more complicated case: The amplitude is modulated by the function $F_x(u')$ already causing a different phase relation of the far-field components. In addition to the above-mentioned phase change due to precession, the far-field polarization quantities Ψ and χ depend also on the amplitude profiles $\tilde{A}_\parallel(u')$ and $\tilde{A}_\phi(u')$.

[1] Y. Yamamoto and R. E. Slusher, Phys. Today **46**(6), 66 (1993).
[2] K. J. Vahala, Nature (London) **424**, 839 (2003).
[3] L. Collot, V. Lefèvre-Seguin, M. Brune, J. M. Raimond, and S. Haroche, Europhys. Lett. **23**, 327 (1993).
[4] M. L. Gorodetsky, A. D. Pryamikov, and V. S. Ilchenko, J. Opt. Soc. Am. B **17**, 1051 (2000).
[5] F. Vollmer, L. Yang, and S. Fainman, Nanophotonics **1**, 267 (2012).
[6] V. S. Ilchenko, M. L. Gorodetsky, X. S. Yao, and L. Maleki, Opt. Lett. **26**, 256 (2001).
[7] D. K. Armani, T. J. Kippenberg, S. M. Spillane, and K. J. Vahala, Nature (London) **421**, 925 (2003).
[8] S. L. McCall, A. F. J. Levi, R. E. Slusher, S. J. Pearton, and R. A. Logan, Appl. Phys. Lett. **60**, 289 (1992).
[9] C. P. Michael, K. Srinivasan, T. J. Johnson, O. Painter, K. H. Lee, K. Hennessy, H. Kim, and E. Hu, Appl. Phys. Lett. **90**, 051108 (2007).
[10] M. Sumetsky, Opt. Lett. **29**, 8 (2004).
[11] C. Strelow, C. M. Schultz, H. Rehberg, H. Welsch, C. Heyn, D. Heitmann, and T. Kipp, Phys. Rev. B **76**, 045303 (2007).
[12] C. Strelow, H. Rehberg, C. M. Schultz, H. Welsch, C. Heyn, D. Heitmann, and T. Kipp, Phys. Rev. Lett. **101**, 127403 (2008).
[13] F. Li, S. Vicknesh, and Z. Mi, Electron. Lett. **45**, 645 (2009).
[14] C. Strelow, C. M. Schultz, H. Rehberg, M. Sauer, H. Welsch, A. Stemmann, C. Heyn, D. Heitmann, and T. Kipp, Phys. Rev. B **85**, 155329 (2012).
[15] L. B. Ma, S. L. Li, V. M. Fomin, M. Hentschel, J. B. Götte, Y. Yin, M. R. Jorgensen, and O. G. Schmidt, Nat. Commun. **7**, 10983 (2016).
[16] G. Huang and Y. Mei, J. Mater. Chem. C **5**, 2758 (2017).
[17] J. Wang, Y. Yin, Y. D. Yang, Q. Hao, M. Tang, X. Wang, C. N. Saggau, D. Karnaushenko, X. Yan, Y. Z. Huang, L. Ma, and O. G. Schmidt, ACS Photon. **6**, 2537 (2019).
[18] S. Lacey and H. Wang, Opt. Lett. **26**, 1943 (2001).
[19] H. G. L. Schwefel, A. D. Stone, and H. E. Tureci, J. Opt. Soc. Am. B **22**, 2295 (2005).
[20] I. Teraoka and S. Arnold, J. Opt. Soc. Am. B **23**, 1381 (2006).
[21] J. Kreismann, S. Sinzinger, and M. Hentschel, Phys. Rev. A **95**, 011801(R) (2017).
[22] J. Kreismann and M. Hentschel, Europhys. Lett. **121**, 24001 (2018).
[23] S. A. Gladyshev, A. A. Bogdanov, P. V. Kapitanova, M. V. Rybin, K. L. Koshelev, Z. F. Sadrieva, K. B. Samusev, Y. S. Kivshar, and M. F. Limonov, J. Phys.: Conf. Ser. **1124**, 51058 (2018).
[24] F. Khosravi, C. L. Cortes, and Z. Jacob, Opt. Express **27**, 15846 (2019).
[25] K. Y. Bliokh and F. Nori, Phys. Rep. **592**, 1 (2015).
[26] A. Aiello, P. Banzer, M. Neugebauer, and G. Leuchs, Nat. Photon. **9**, 789 (2015).
[27] F. Cardano and L. Marrucci, Nat. Photon. **9**, 776 (2015).
[28] C. Junge, D. O'Shea, J. Volz, and A. Rauschenbeutel, Phys. Rev. Lett. **110**, 213604 (2013).
[29] D. O'Connor, P. Ginzburg, F. J. Rodríguez-Fortuño, G. A. Wurtz, and A. V. Zayats, Nat. Commun. **5**, 5327 (2014).
[30] Z. Shao, J. Zhu, Y. Chen, Y. Zhang, and S. Yu, Nat. Commun. **9**, 926 (2018).
[31] J. S. Eismann, P. Banzer, and M. Neugebauer, Phys. Rev. Research **1**, 033143 (2019).
[32] A. T. Rosenberger, E. B. Dale, K. V. Bui, E. K. Gonzales, D. Ganta, L. Ke, and S. R. Rajagopal, Opt. Lett. **44**, 4163 (2019).
[33] L. Sun, B. Bai, J. Wang, M. Zhang, X. Zhang, X. Song, and L. Huang, Adv. Funct. Mater. **29**, 1902286 (2019).
[34] M. V. Berry, Proc. R. Soc. London Ser. A **392**, 45 (1984).
[35] M. V. Berry, Nature (London) **326**, 277 (1987).
[36] K. Y. Bliokh, A. Niv, V. Kleiner, and E. Hasman, Nat. Photon. **2**, 748 (2008).
[37] K. Y. Bliokh, M. A. Alonso, and M. R. Dennis, Rep. Prog. Phys. **82**, 122401 (2019).
[38] D. Loss, P. Goldbart, and A. V. Balatsky, Phys. Rev. Lett. **65**, 1655 (1990).
[39] F. Nagasawa, D. Frustaglia, H. Saarikoski, K. Richter, and J. Nitta, Nat. Commun. **4**, 2526 (2013).
[40] D. Frustaglia, M. Hentschel, and K. Richter, Phys. Rev. Lett. **87**, 256602 (2001).
[41] M. Hentschel, H. Schomerus, D. Frustaglia, and K. Richter, Phys. Rev. B **69**, 155326 (2004).
[42] *Classical Electrodynamics*, 3rd ed., edited by J. D. Jackson (Wiley, New York, 1998).
[43] V. A. Bolaños Quiñones, G. Huang, J. D. Plumhof, S. Kiravittaya, A. Rastelli, Y. Mei, and O. G. Schmidt, Opt. Lett. **34**, 2345 (2009).
[44] V. A. Bolaños Quiñones, L. Ma, S. Li, M. Jorgensen, S. Kiravittaya, and O. G. Schmidt, Opt. Lett. **37**, 4284 (2012).
[45] E. Collett, *Field Guide to Polarization* (SPIE, Bellingham, 2005).
[46] A. F. Oskooi, D. Roundy, M. Ibanescu, P. Bermel, J. D. Joannopoulos, and S. G. Johnson, Comput. Phys. Commun. **181**, 687 (2010).
[47] R. K. D. Colton, *Inverse Acoustic and Electromagnetic Scattering Theory* (Springer, Berlin, 1998), p. 32.
[48] F. W. A. Shapere, *Geometric Phases in Physics* (World Scientific, Singapore, 1989), Vol. 5, pp. 45–104 and 193–240.